PHYSICAL REVIEW B **84**, 014105 (2011)

Developing grain boundary diagrams as a materials science tool: A case study of nickel-doped molybdenum

Xiaomeng Shi[1,*] and Jian Luo[1,2,†]
[1]*School of Materials Science and Engineering,*
[2]*Center for Optical Materials Science and Engineering Technologies, Clemson University, Clemson, South Carolina 29634, USA*

(Received 23 February 2011; published 20 July 2011)

Impurity-based, premelting-like, grain boundary (GB) "phases" (complexions) can form in alloys and influence sintering, creep, and microstructural development. Calculation of Phase Diagrams (CalPhaD) methods and Miedema-type statistical interfacial thermodynamic models are combined to forecast the formation and stability of subsolidus quasiliquid GB phases in binary alloys. This work supports a long-range scientific goal of developing "GB (phase) diagrams" as a new materials science tool to help controlling the materials fabrication processing and resultant materials properties. Using nickel-doped molybdenum as a model system, a type of GB diagram (called "λ diagram") is computed to represent the temperature- and composition-dependent thermodynamic tendency for general GBs to disorder. Subsequently, controlled sintering experiments are conducted to estimate the GB diffusivity as a function of temperature and overall composition, and the experimental results correlate well with the computed GB diagram. Although they are not yet rigorous GB-phase diagrams with well-defined transition lines, the predictability and usefulness of such λ diagrams are demonstrated. Related interfacial thermodynamic models and computational approaches are discussed.

DOI: 10.1103/PhysRevB.84.014105 PACS number(s): 61.72.Mm, 05.70.Np, 68.35.Dv, 81.05.Bx

I. INTRODUCTION

Interfacial phase formation and transition can often play vital roles in microstructural development and determine the resultant materials properties. The existence of various surface transitions, such as premelting (formation of quasiliquid interfacial structures),[1] prewetting (adsorption transitions),[2] layering (step-wise adsorption in the multilayer regime),[3] and reconstruction (change of surface symmetry) has been well established; consequently, a variety of surface "phase" diagrams have been constructed and proven useful. While surface science has advanced significantly, the interfacial science for grain boundaries (GBs) has lagged. Recent studies suggested that in multicomponent alloys, coupled structural (premelting) and adsorption (prewetting) transitions can occur at GBs.[4–9] Thermodynamic theories have been developed to treat GBs as regions of distinct interfacial phases,[5,7,10] and a series of generic GB phases have been identified and named as complexions.[5,10,11] While the existence of surface phases is well established,[3] the identification of GB analogs at internal interfaces shed light on several long-standing mysteries in materials science regarding the origins of solid-state activated sintering,[12,13] abnormal grain growth,[5,10] and liquid metal embrittlement.[14]

One ubiquitous GB complexion (phase) is represented by the impurity-based intergranular films (IGFs). Such nanoscale IGFs have been observed at GBs in numerous ceramic materials,[8] WC-Co cermet,[15] and several metal alloys including W-Ni,[13,16] Mo-Ni,[17] and Nd-Fe-B,[18] where the nanoscale amorphous (quasiliquid) IGFs were directly observed by high-resolution transmission electron microscopy (HRTEM), and Cu-Bi[19] and Fe-Si-Zn,[20,21] where their existence was suggested by diffusivity measurements. Nanometer-thick films of similar character have also been observed on free surfaces in oxides,[22] as well as at ceramic-ceramic[8] and metal-oxide[23–27] phase boundaries. These interfacial films adopt self-selecting or equilibrium thickness on the order of one nanometer. Thus, they are not complete wetting films (which should exhibit arbitrary thickness); instead, they can be considered as prewetting films (the relevant terminologies were discussed in a recent critical review article).[8] Moreover, when the effective interfacial width is comparable with the atomic size, layering transitions can occur[28] and produce a series of additional discrete GB phases such as monolayers, bilayers, and trilayers, which are known as Dillon-Harmer complexions.[5,10,11]

Furthermore, impurity-based quasiliquid GB phases or IGFs can often be stabilized well below the bulk solidus lines, where the liquid phases are not yet stable bulk phases.[8,13,16,17,29–31] In such cases an analogy to the phenomenon of premelting in unary systems[1] can be drawn. The formation of premelting-like GB phases can significantly affect materials fabrication processing, microstructural evolution, and high-temperature materials properties. As one specific example, enhanced diffusion in quasiliquid GB phases (IGFs) explained the origin of solid-state (subsolidus) activated sintering, which refers to the significant enhancement of densification rates by addition of a small amount of sintering aids (dopants) at the temperatures well below bulk solidus lines in ceramic materials[8,29–31] and refractory metals.[13,16,17] In a recent letter[32] a thermodynamic model was proposed, which predicted that quasiliquid IGFs can be stabilized at as low as 60–85% of the bulk solidus temperatures in certain systems such as Pd- or Ni-doped W. A primitive type of GB diagram was developed to represent the stability of subsolidus quasiliquid IGFs. The predicted GB-disordering temperatures were coincident with the experimentally observed onset sintering temperatures for all five binary W alloys, for which both thermodynamic parameters and experimental data are available. More recently a revised, analytical approach was proposed to estimate IGF thickness for regular-solution solid phases, and this approach was verified partially by direct

HRTEM characterization of Ni-doped Mo.[17] However, a critical and systematical validation of a computed GB diagram with the temperature and composition dependent experimental data has not yet been conducted, which motivated this study.

This paper systematically discusses the interfacial-thermodynamic models and approaches to compute GB diagrams for binary alloys; several improvements for the models and computation methods are proposed and validated. Ni-doped Mo is selected as the model system because a prior HRTEM study directly confirmed the stabilization of quasiliquid IGFs below the solidus line,[17] and the verification of a counterintuitive prediction that a retrograde solubility of Ni in Mo can lead to a decrease in the GB diffusivity with increasing temperature further supported the existence of premelting-like IGFs in this system.[33] A primitive type of GB diagram (called λ diagram) is computed for Ni-doped Mo. Furthermore, systematical sintering experiments are conducted to estimate the GB diffusivity as a function of temperature and Ni content, which provide the most systematic model-experimental validation to date.

While diffuse-interface (phase-field) models have been recently developed to compute more rigorous GB "phase" diagrams with well-defined transition lines and critical points for a GB of a specific crystallographic inclination and misorientation in a binary alloy,[7,34] this work adopts a simpler sharp-interface approach to robustly compute the thermodynamic tendency for (average) general GBs to disorder. Two related computational approaches are discussed; the emphasis of this paper is placed on an approximate approach that leads to analytical solutions for regular-solution and subregular-solution solid phases for the sake of easy implementation. The computed λ diagrams, although they are not rigorous GB "phase" diagrams, can be readily quantified for realistic materials systems, thereby being practically useful. This study systematically demonstrates the correctness and usefulness of such a computed λ diagram and the underlying interfacial thermodynamic models for a binary transition metal alloy, which establishes a solid basis to develop models and approaches for computing GB diagrams for more complex multicomponent alloys and/or ceramic systems in future studies. Thus, this study represents an important step toward a long-range scientific goal of developing "GB (phase) diagrams" as a general materials science tool to help achieving predictive fabrication of materials by design.

II. THERMODYNAMIC MODELS

A. A phenomenological model

A phenomenological interfacial thermodynamic model can be derived by extending a sharp-interface premelting model for unary systems.[1,35] In this model for binary alloys the excess GB energy [using the equilibrium bulk phase(s) as the reference state(s)] of a subsolidus liquidlike IGF in a binary A-B alloy is expressed as[8,12]

$$\begin{aligned}\sigma^x(h) &\equiv G^S - (\mu_A\Gamma_A + \mu_B\Gamma_B)\\ &= 2\gamma_{\mathrm{cl}} + \Delta G^{(\mathrm{vol})}_{\mathrm{amorph}}\cdot h + \sigma_{\mathrm{interfacial}}(h),\end{aligned} \quad (1)$$

where G^S is the excess free energy according to the Gibbs definition, μ_A and μ_B are the bulk chemical potentials, Γ_A and Γ_B are the GB excesses, h is the film thickness, γ_{cl} is the interfacial energy of the crystal-liquid interface (which is well defined when the two interfaces are well separated or $h \to +\infty$), and $\Delta G^{(\mathrm{vol})}_{\mathrm{amorph}}$ is the (volumetric) free-energy penalty for forming an undercooled liquid. The last term in Eq. (1) is an *interfacial potential* that represents the interactions of two interfaces when the film is thin; it is the sum of all short- and long-range interfacial interactions using $h = +\infty$ as the reference point, and its derivative $(d\sigma_{\mathrm{interfacial}}/dh)$ is the well-known *Derjaguin disjoining pressure*. By definition,

$$\begin{cases}\sigma_{\mathrm{interfacial}}(0) = \left(\gamma^{(0)}_{gb} - 2\gamma_{\mathrm{cl}}\right) \equiv -\Delta\gamma\\ \sigma_{\mathrm{interfacial}}(+\infty) = 0\end{cases}, \quad (2)$$

where we define $\gamma^{(0)}_{gb} \equiv \sigma^x(0)$ as the excess free energy of a hypothetical "dry" GB. Here the superscript (0) is used to denote that $\gamma^{(0)}_{gb}$ is different from the equilibrium γ_{gb}, which corresponds to the global minimum in $\sigma^x(h)$ that satisfies

$$\begin{cases}\left.\frac{d\sigma^x(h)}{dh}\right|_{h=h_{\mathrm{eq.}}} = 0\\ \gamma_{gb} \equiv \sigma^x(h_{\mathrm{eq}})\end{cases}, \quad (3)$$

where h_{eq} is the so-called equilibrium thickness. One may further define a dimensionless *interfacial coefficient* as

$$f(h) \equiv 1 + \frac{\sigma_{\mathrm{interfacial}}(h)}{\Delta\gamma}, \quad (4)$$

which satisfies

$$\begin{cases}f(0) = 0\\ f(+\infty) = 1\end{cases}. \quad (5)$$

Then Eq. (1) can be rewritten as

$$\Delta\sigma(h) \equiv \sigma^x(h) - \gamma^{(0)}_{gb} = \Delta\gamma\cdot f(h) + \Delta G^{(\mathrm{vol})}_{\mathrm{amorph}}\cdot h, \quad (6)$$

where the reference state is set to be the case of $h = 0$ [i.e., $\Delta\sigma(0) \equiv 0$]. A quasiliquid IGF of thickness h can be thermodynamically more stable than a dry GB if $\Delta\sigma(h) < 0$ or

$$\Delta G^{(\mathrm{vol})}_{\mathrm{amorph}}\cdot h < -\Delta\gamma\cdot f(h). \quad (7)$$

To estimate the IGF thickness, we define[17]

$$\lambda \equiv -\Delta\gamma/\Delta G^{(\mathrm{vol})}_{\mathrm{amorph}}, \quad (8)$$

which represents the thermodynamic tendency for general (average, low-symmetry, random) GBs to disorder. In a binary alloy the value of this λ depends on the (somewhat subjective) selection of a reference film composition, and possible strategies are discussed subsequently. If the interfacial potential follows a simple exponentially decaying form, liquidlike GB structures will form when $\lambda_L > \xi$ with an effective width $h_{\mathrm{eq}} = \xi\cdot\ln(\lambda_L/\xi)$, where ξ is a coherent length on the order of the atomic size. The realistic interfacial potentials for multicomponent alloys can be more complex because of the existence of multiple interfacial interactions. For ceramic materials long-range van der Waals London dispersion forces and electrostatic interactions, which should also be included in the interfacial potential term, can often play significant roles and give rise to even more complex interfacial phase behaviors.

B. Through-thickness gradients, film composition, and simplifications

Through-thickness compositional (and structural) gradients generally exist in a nanometer-thick quasiliquid IGF sandwiched between two crystalline grains. Correspondingly one may select the average film composition as a reference film composition to compute ΔG_{amorph}. However, this average film composition, which is a function of film thickness, is not known *a priori*. Alternatively one may make a somewhat subjective selection of a reference film composition for a hypothetical uniform film of undercooled liquid; the remaining volumetric free energies, along with the excess free energies associated with the compositional and structural gradients, can be considered in the interfacial potential so that the thermodynamic treatment remains rigorous.

Furthermore, computing the equilibrium γ_{cl} should consider the effects of the near-interface gradients in composition (adsorption) and structure (partial ordering). In a rigorous approach γ_{cl} should be defined for the case of $h \to \infty$ and with respect to a reference composition of $X_L{}^*$ that minimizes ΔG_{amorph}. Practically, it is rather difficult to quantify this equilibrium γ_{cl}. Thus, in this paper and prior studies,[12,17,32] an unrelaxed $\gamma_{\text{cl}}^{(0)}$ for a hypothesized step interface between a crystal and a perfect liquid (without a compositional gradient) is adopted as a useful approximation. Here the superscript (0) is used to denote that this unrelaxed $\gamma_{\text{cl}}^{(0)}$ is different (smaller) than the true (equilibrium) γ_{cl} with the same reference composition. This unrelaxed $\gamma_{\text{cl}}^{(0)}$ is a function of the (subjectively selected) composition. The relevant models and equations are given subsequently.

Thus, the λ defined in Eq. (9) becomes a function of the reference film composition

$$\lambda_X\left(X_{\text{film}}^{(\text{ref})}\right) \equiv \frac{\gamma_{gb}^{(0)} - 2\gamma_{\text{cl}}^{(0)}\left(X_{\text{film}}^{(\text{ref})}\right)}{\Delta G_{\text{amorph}}\left(X_{\text{film}}^{(\text{ref})}\right)}. \tag{9}$$

The consistence of the thermodynamic model requires this reference composition to be identical to the liquidus composition (X_L) as h (or λ) approaches $+\infty$. Several possible conventions that can satisfy this requirement are discussed as follows. The simplest convention is to select X_L as the reference film composition. Although this convention leads to an unphysical solution for pure A, this problem can be remedied, as discussed subsequently. A key advantage for adopting this simplified convention is that it leads to (almost) analytical solutions for ΔG_{amorph}. Alternatively this reference film composition can be selected to maximize a particular figure of merit; here the two most natural choices are to select this reference film composition to minimize ΔG_{amorph} (i.e., to maximize the figure of merit of $1/\Delta G_{\text{amorph}}$) or to maximize λ itself,[12,32] respectively. These three conventions will lead to somewhat different definitions of λ, as follows:

$$\begin{cases} \lambda_L \equiv \lambda_X(X_L) \\ \lambda^* \equiv \lambda_X(X_L^*) \ \ (\text{where} X_L^* \text{minimizes} \Delta G_{\text{amorph}}) \\ \lambda \equiv \underset{(0<X_{\text{film}}^{(\text{ref})}<1)}{\text{Max}} \left\{\lambda_X\left(X_{\text{film}}^{(\text{ref})}\right)\right\} \end{cases} \tag{10}$$

It is easy to demonstrate that

$$\lambda_L \leqslant \lambda^* \leqslant \lambda. \tag{11}$$

All the reference film compositions should be identical to X_L at the limit of $h \to +\infty$, so that

$$\lim_{\lambda \to +\infty} \frac{\lambda_L}{\lambda} = \lim_{\lambda \to +\infty} \frac{\lambda^*}{\lambda} = 1. \tag{12}$$

All three λ's represent the thermodynamic tendency to stabilize subsolidus liquidlike IGFs, and they scale the actual film thickness. Since the exact form of the interfacial potential is generally unknown, none of them can guarantee more predictive power than others. While λ^* and λ appear to be conceptually more rigorous, λ_L is easier to quantify. In prior studies[12,32] we quantified λ via a numerical method. More recently we derived an analytical solution for ΔG_{amorph} and λ_L for regular solution-solid phases.[17] In this paper we further derived the analytical solutions for solid phases that are represented by subregular solutions. In the subsequent sections we will show that the numerical values of λ and λ_L are typically close to each other (noting that $\lambda_L \leqslant \lambda^* \leqslant \lambda$).

In summary λ_L, which is the maximum thickness of a stable IGF assuming a uniform film composition of X_L and no interfacial interactions, appears to be the most convenient thermodynamic variable to be used practically. Thus, it is adopted in this study. To compute λ_L as a function of temperature and bulk composition, both interfacial energies and bulk-free energies need to be quantified, which are discussed in the following sections.

C. Estimation of interfacial energies

The interfacial energies (γ's) can be estimated by lattice-gas models or Miedema-type macroscopic-atom models. In a commonly used lattice-gas model if the solubility of B in solid (crystalline) A is negligible, the crystal-liquid interfacial energy can be expressed as

$$\gamma_{\text{cl}}^{(0)} = \underbrace{\gamma_{\langle A\rangle-\{A\}}}_{(\text{enthalpic})} + \underbrace{\frac{m_1\omega_L}{V^{2/3}}(X_B)^2}_{(\text{interaction})}, \tag{13}$$

where X_B is the atomic fraction of B in the liquid, ω_{L} is the regular solution parameter for the liquid phase, m_1 is the fraction of the (liquid-type) bonds that cross the crystal-liquid interface, and V is molar volume. In Eq. (13) the first term ($\gamma_{\langle A\rangle-\{A\}}$ or the crystal-liquid interfacial energy of pure A) represents an enthalpic contribution, and the second term is a chemical interaction term resulted from the formation of a different number of A-B bonds at the interfaces as compared to those in the bulk liquid. This lattice-gas model assumes that the solid-liquid interface can be represented by a step function and that the bonds at the interface are liquid type. If the solubility of B in an A crystal is not negligible, a more general expression of Eq. (13) can be found in Ref. 36.

Although the above lattice-gas model is more general and commonly used, in this work we adopt and further modify a Miedema-type macroscopic-atom model to estimate interfacial energies. This macroscopic-atom model, which was developed by Mittemeijer and coworkers[37,38] on a similar base as lattice-gas models, is more realistic to represent binary transition-metal alloys. This model considers the different molar volumes for A and B, represents average general interfaces without anisotropic effects (which suits the objective of this study), and provides a systematical method to evaluate the required thermodynamic parameters. In the original model developed by Benedictus, Böttger, and Mittemeijer (BBM)[37,38] the interfacial energy for an A crystal (with negligible solubility of B) and a binary A-B liquid is expressed as

$$\gamma_{\rm cl}^{(0,BBM)} = \underset{\text{(Enthalpic)}}{\underline{\frac{H_{\rm A}^{\rm fuse}}{C_0 V_A^{2/3}}}} + \underset{\text{(Interaction)}}{\underline{\frac{\Delta H^{\rm interface}_{{\rm Ain}B} F_B^A}{C_0 V_A^{2/3}}}} + \underset{\text{(Entropic)}}{\underline{\frac{1.9RT}{C_0 V_{A/B}^{2/3}}}}, \tag{14}$$

where $H_A^{\rm fuse}$ is the fusion enthalpy of A, $\Delta H^{\rm interface}_{{\rm Ain}B}$ is the enthalpy of solution of A in B, $C_0 \approx 4.5 \times 10^8$, V is the molar volume (neglecting thermal expansion), R is the gas constant, and F_B^A represents the "area" fraction A-B bonds at the interface, which is expressed as

$$F_B^A = \frac{X_B V_B^{2/3}}{(1 - X_B)V_A^{2/3} + X_B V_B^{2/3}}, \tag{15}$$

where X_B is the atomic fraction of B in the liquid phase.

It should be noted that the interaction term in Eq. (14) has been derived assuming that the reference states are pure crystal A and pure crystal B (which is perfectly valid for modeling the solid-state amorphization that starts from pure A and B crystals, which was the objective for BBM's original work[37,38]). In the present case, however, the thermodynamic equilibrium state (solid and liquid solutions) should be used as the reference state. To modify the model, let us consider a hypothetical interface between two liquids of the same composition, which should theoretically have zero excess free energy. However, this interface has a nonzero interaction term in the BBM model as

$$\gamma_{\rm liq-liq.}^{\rm (Ref.)} = \frac{\Delta H^{\rm interface}_{{\rm Ain}B}}{C_0 V_A^{2/3}}\left[2F_B^A \cdot \left(1 - F_B^A\right)\right], \tag{16}$$

where $[2F_B^A \cdot (1 - F_B^A)]$ represents the area fraction of A-B bonds for this hypothetical liquid-liquid interface. Thus, Eq. (14) should be revised to

$$\gamma_{\rm cl}^{(0)} = \underset{\text{(Enthalpic)}}{\underline{\frac{H_{\rm A}^{\rm fuse}}{C_0 V_A^{2/3}}}} + \underset{\text{(Interaction)}}{\underline{\left[\frac{\Delta H^{\rm interface}_{{\rm Ain}B} F_B^A}{C_0 V_A^{2/3}} - \frac{1}{2}\gamma_{\rm liq-liq.}^{\rm (Ref.)}\right]}} + \underset{\text{(Entropic)}}{\underline{\frac{1.9RT}{C_0 V_{A/B}^{2/3}}}} \tag{17}$$

or

$$\gamma_{\rm cl}^{(0)} = \underset{\text{(Enthalpic)}}{\underline{\frac{H_A^{\rm fuse}}{C_0 V_A^{2/3}}}} + \underset{\text{(Interaction)}}{\underline{\frac{\Delta H^{\rm interface}_{{\rm Ain}B} (F_B^A)^2}{C_0 V_A^{2/3}}}} + \underset{\text{(Entropic)}}{\underline{\frac{1.9RT}{C_0 V_{A/B}^{2/3}}}}. \tag{18}$$

Note that the first two terms in Eq. (18) correspond to the two terms in the lattice-gas model [Eq. (13)], and they are modified terms after considering the different molar volumes. In fact here we have derived the modification of the interaction term in Eq. (18) based on an analogy to the lattice-gas model [as shown in Eq. (13) and Ref. 36]. In addition to enthalpic and interaction contributions an entropic contribution is also included in Eq. (18).

Specific to the Mo-Ni binary system of our interest, the liquid-crystal interfacial energy is determined as

$$\gamma_{\rm cl}^{(0)} = \left\{0.138 - 0.160\left[X_{\rm Ni}^L/\left(1.253 - 0.253X_{\rm Ni}^L\right)\right]^2 + 8.92 \times 10^{-5}T\right\}{\rm J/m}^2. \tag{19}$$

On the other hand the average GB energy of Mo is determined following the Turnbull's estimation

$$\gamma_{gb}^{(0)} \approx \frac{1}{3} \cdot \gamma_{\rm Mo}^{\rm surface} = \frac{1}{3} \cdot \frac{H_{\rm Mo}^{\rm vap}}{C_0 V_{\rm Mo}^{2/3}} = 1.0{\rm J/m}^2, \tag{20}$$

where the thermal expansion is ignored. Noting that Eq. (20) also assumes that the solubility of Ni in solid Mo (BCC phase) is negligible; if the solid phase has substantial solubility of the alloying element(s), a more general equation for $\gamma_{gb}^{(0)}$ should be derived and used.

This macroscopic-atom model can be further refined in several grounds by adopting strategies and approaches developed in several refined lattice-gas models. First, as we have discussed previously, this model can be extended to consider cases where the solubility of B in an A crystal is not negligible following a scheme used in a lattice-gas model.[36] Second the adsorption at the liquid-crystal interface and the associated compositional gradient may be considered using an approach similar to a model proposed by Shimizu and Takei,[39,40] which can be further refined. Third the solute segregation within the lattice and anisotropic effects may be considered following a model developed by Wynblatt *et al.*[41] Fourth the asymmetric effects represented by subregular solutions can be considered by adopting the approach similar to a model proposed by Antion and Chatain.[42] A further refinement should also consider the partial crystallinity and structural gradients, which will eventually lead to more sophisticated diffuse-interface models.[4–9]

D. Free-energy penalty for forming an undercooled liquid

The Calculation of Phase Diagram (CalPhaD) methods are adopted to determine the free-energy penalty to form an undercooled liquid ($\Delta G_{\rm amorph}$). CalPhaD is a set of well-established methods to compute bulk-phase diagrams from (usually empirically fitted) thermodynamic functions of free energies. The Gibbs free energy of a phase Φ in a binary A-B system can be expressed as

$$G^\Phi = \sum_{i=A,B} X_i \cdot {}^0G_i^\Phi + RT \sum_{i=A,B} X_i \ln X_i + {}^{XS}G^\Phi, \tag{21}$$

where ${}^0G_i^\Phi$ is the Gibbs free energy of the pure element $i\,(=A \text{ or } B)$ that is present in Φ phase, X_i is the atomic fraction of element i, and ${}^{XS}G^\Phi$ is the excess Gibbs free energy, which can be empirically expressed in a Redlich-Kister polynomial

$${}^{XS}G^\Phi = X_A X_B \sum_{j=0}^{n} L_j^\Phi (X_A - X_B)^j. \tag{22}$$

Here, L_j^Φs are empirically fitted parameters for the phase Φ. If $n = 0$ the phase Φ is a regular solution, and Eq. (22) is reduced to

$$^{XS}G^\Phi = L_0^\Phi X_A X_B \equiv \omega X_A X_B, \tag{23}$$

where ω ($=L_0^\Phi$) is the regular solution parameter. If $\omega = 0$ the phase Φ is an ideal solution ($^{XS}G^\Phi = 0$).

If $n = 1$ the phase Φ is a subregular solution. Equation (22) can be rewritten as

$$^{XS}G^\Phi = L_0^\Phi X_A X_B + L_1^\Phi X_A X_B (X_A - X_B). \tag{24}$$

Gibbs free-energy functions for compounds and ordered solutions can be constructed using different models. For a given binary A-B system the Gibbs free-energy functions can be developed for all possible phases. Then a bulk-phase diagram can be constructed by minimizing the total free energy of the system. In two-phase regions the equilibrium states can be found graphically via a well-established "common tangent construction" method.

For the Mo-Ni binary system four phases (BCC, FCC, δ-NiMo, and liquid) are typically considered. The Gibbs free energies of different phases have been obtained in Refs. 43 and 44, whereas only the functions in Ref. 43 are adopted in this study because they lead to better predictions of the solidus and solvus lines of the Mo-rich BCC as well as the peritectic temperature. The specific thermodynamic functions used here can also be found in Ref. 43.

The CalPhaD methods are used to compute ΔG_{amorph} and subsequently λ_L. From now on all the X's (X, X_{film}, X_S, X_L) in equations are referred to as atomic fractions of Ni in the Ni-Mo binary system, and the subscript B or Ni is dropped for brevity. The specific definitions are given as follows.

1. X is the (general) Ni fraction,
2. X_{film} is the Ni fraction of the IGF,
3. X_0 is the Ni fraction of the bulk (BCC) phase (which sets the bulk chemical potentials or the reference state),
4. X_S is the Ni fraction on the solidus line or (if $T < T_{\text{preitectic}}$) its metastable extension,
5. X_L is the Ni fraction on the liquidus line or (if $T < T_{\text{preitectic}}$) its metastable extension, and
6. X_{solvus} is the Ni fraction on the solvus line (for $T < T_{\text{preitectic}}$).

Here we show that an analytical expression for λ_L can be obtained if we assume the solid (BCC) phase is a regular or subregular solution, for which the (molar) Gibbs energy is given by

$$\begin{aligned} G^{\text{bcc}} = {} & X_0 \cdot {}^0G_{Ni}^{\text{bcc}} + (1 - X_0) \cdot {}^0G_{\text{Mo}}^{\text{bcc}} \\ & + RT[X_0 \ln X_0 + (1 - X_0)\ln(1 - X_0)] \\ & + L_0^{\text{bcc}} X_0(1 - X_0) + L_1^{\text{bcc}} X_0(1 - X_0)(1 - 2X_0). \end{aligned} \tag{25}$$

First let us determine the ΔG_{amorph} in the single-phase (BCC) regime. Figure 1 shows an example at $T = 1450\,^\circ\text{C}$ ($T > T_{\text{peritectic}}$), in which the composition of the bulk BCC phase (X_0) is lower than the bulk-solidus composition (X_S). As shown in Fig. 1(a) the ΔG_{amorph} is defined as the difference between of the metastable-liquid phase (the red line) and the reference-state set by the chemical potential of the stable bulk phase of a composition X_0. This reference state is given by

$$\begin{aligned} G^{\text{Ref.}}(X) &= X_{\text{film}} \cdot \mu_{Ni} + (1 - X_{\text{film}}) \cdot \mu_{\text{Mo}} \\ &= G^{\text{bcc}}(X_0) + (X_{\text{film}} - X_0) \left.\frac{dG^{\text{bcc}}}{dX}\right|_{X=X_0}, \end{aligned} \tag{26}$$

which corresponds to the tangent line extended from X_0 [as being labeled in Fig. 1(a)]. Thus, the molar free-energy penalty to form a metastable liquid of composition X_L [being labeled by a purple double arrow in Fig. 1(a)] is given by

$$\begin{aligned} &\Delta G_{\text{amorph}}^{(\text{mol})} \\ &\quad = G^{\text{liq}}(X_L) - \left[G^{\text{bcc}}(X_0) + (X_L - X_0) \left.\frac{dG^{\text{bcc}}}{dX}\right|_{X=X_0} \right], \end{aligned} \tag{27}$$

where G^{liq} and G^{bcc} are the formation-free energies of liquid and solid BCC phases, respectively. The superscript (mol) denotes it is a molar-free energy, and it relates to the volumetric-free energy by

$$\Delta G_{\text{amorph}}^{(\text{vol})} \approx \Delta G_{\text{amorph}}^{(\text{mol})} / [V_{Ni} \cdot X_L + V_{\text{Mo}} \cdot (1 - X_L)], \tag{28}$$

where V_{Ni} and V_{Mo} are the molar volumes; it is assumed that the film adopts the liquidus composition, and the mixing volume is equal to zero.

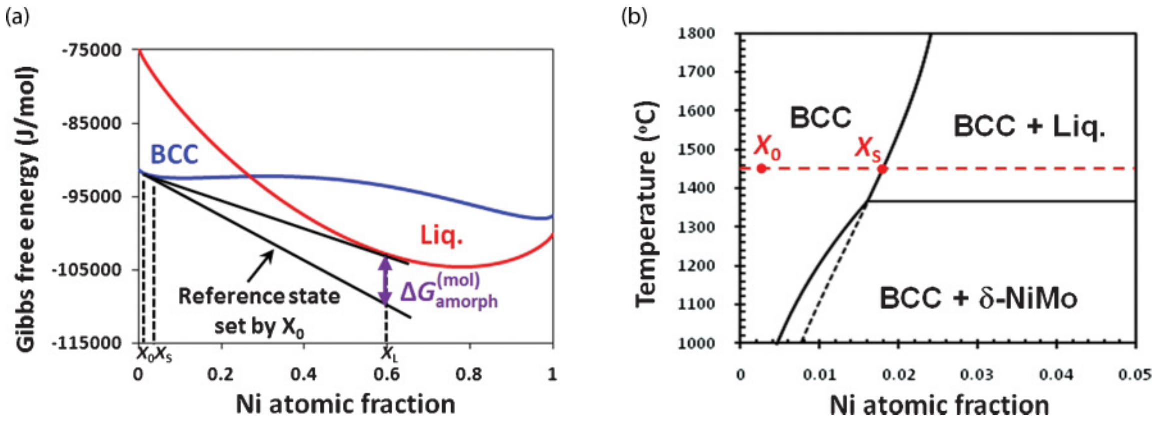

FIG. 1. (Color online) (a) Illustration of ΔG_{amorph} (X_L) in the Gibbs free energy vs Ni-fraction plots for a case of $X_0 < X_S$ and $T = 1450\,^\circ\text{C}$ ($> T_{\text{peritectic}}$). (b) The Mo-rich portion of the corresponding binary bulk-phase diagram.

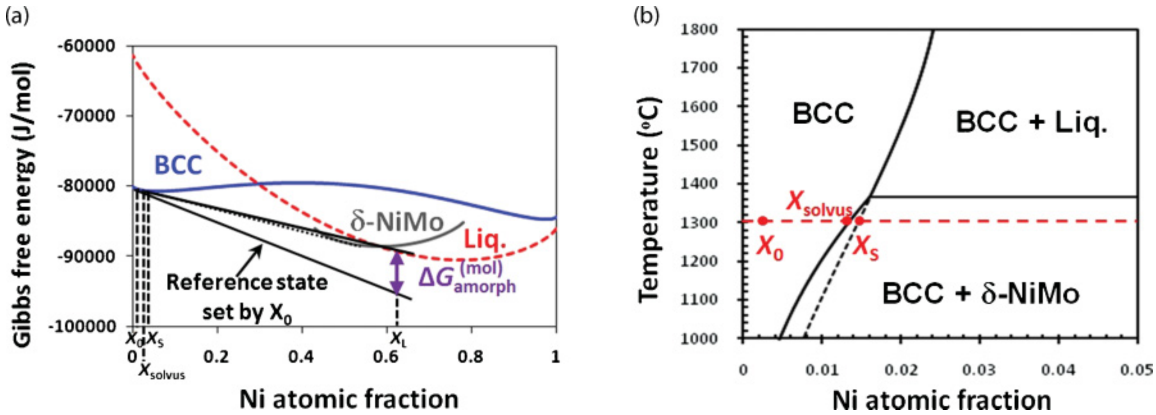

FIG. 2. (Color online) (a) Illustration of ΔG_{amorph} (X_L) in the Gibbs free energy vs Ni-fraction plots for a case of $X_0 < X_{\text{solvus}}$ and $T = 1300\,^\circ\text{C}$ ($<T_{\text{peritectic}}$). (b) The Mo-rich portion of the corresponding binary bulk-phase diagram.

By definition ΔG_{amorph} vanishes if the composition of the solid BCC phase is on the bulk solidus line ($X_0 = X_S$), which is the case represented by the common tangent line between X_S and X_L in Fig. 1(a); thus,

$$G^{\text{liq}}(X_L) = G^{\text{bcc}}(X_S) + (X_L - X_S)\left.\frac{dG^{\text{bcc}}}{dX}\right|_{X_S}. \qquad (29)$$

Combining Eqs. (26)–(29) and assuming $X_{\text{film}} = X_L$ produces

$$\begin{aligned}\Delta G^{(\text{mol})}_{\text{amorph}} = RT\left[X_L \ln\frac{X_s}{X_0} + (1-X_L)\ln\frac{1-X_s}{1-X_0}\right.\\ - (X_S - X_0)\big[2X_L\big(L_0^{\text{bcc}} + 3L_1^{\text{bcc}}\big)\\ - \big(L_0^{\text{bcc}} + 3L_1^{\text{bcc}} + 6L_1^{\text{bcc}}\big)(X_S + X_0)\\ \left. + 4L_1^{\text{bcc}}\big(X_S^2 + X_S X_0 + X_0^2\big)\big]\right]. \qquad (30)\end{aligned}$$

For a general case the parameters for the BCC phase (L_1^{bcc} and L_0^{bcc}) in Eq. (30) should be replaced by the corresponding parameters for the specific solid phase of interest. If the solid phase is a regular solution ($L_1^{\text{bcc}} = 0$, $L_0^{\text{bcc}} = \omega$), Eq. (30) can be reduced to

$$\begin{aligned}\Delta G^{(\text{mol})}_{\text{amorph}} = RT\left[X_L \ln\frac{X_s}{X_0} + (1-X_L)\ln\frac{1-X_s}{1-X_0}\right]\\ - \omega(X_S - X_0)(2X_L - X_S - X_0). \qquad (31)\end{aligned}$$

This analytical solution for a regular-solution solid phase [Eq. (31)] has been previously given in Ref. 17, and the general analytical solution for a subregular-solution solid phase [Eq. (30)] is derived here for the first time. This approach is almost analytical (except that it assumes that X_S and X_L are known, which have to be determined by either experiments or CalPhaD methods).

Second, in the single BCC phase regime below $T_{\text{peritectic}}$, the procedure for calculating ΔG_{amorph} is essentially the same as that described above for the case of $T > T_{\text{peritectic}}$. Figure 2 illustrates an example for a case of $T = 1300\,^\circ\text{C}$. The only difference is that X_S and X_L are now the Ni fractions on the metastable extensions of the solidus and liquidus lines. In the case of $T < T_{\text{peritectic}}$ the solid solubility limit corresponds to the solvus line X_{solvus} (instead of the metastable X_S).

Finally in the subperitectic two-phase regime, ΔG_{amorph} (X_L) is a constant at a specific temperature, and it does not depend on the overall bulk composition because the bulk chemical potential is a constant in this two-phase region (Fig. 3). Therefore, for a regular-solution solid phase, the free-energy penalty for forming an undercooled liquid can be determined by assuming $X_0 = X_{\text{solvus}}$ in Eq. (31), as

$$\begin{aligned}\Delta G^{(\text{mol})}_{\text{amorph}} = RT\left[X_L \ln\frac{X_s}{X_{\text{solvus}}} + (1-X_L)\ln\frac{1-X_s}{1-X_{\text{solvus}}}\right]\\ - \omega(X_S - X_{\text{solvus}})(2X_L - X_S - X_{\text{solvus}}), \qquad (32)\end{aligned}$$

where X_S refers to the composition on the metastable extension to the solidus line. A similar equation can be readily obtained for a subregular-solution solid phase by substituting X_0 with X_{solvus} in Eq. (30). In the subperitectic two-phase regime the lines of constant λ_L are horizontal lines, which can be constructed graphically by finding the intersections of lines of constant λ_L in the single-phase region and the solvus line, as illustrated in Fig. 3(b).

Figure 4 shows computed λ_L and λ vs Ni-atomic fraction curves at two representative temperatures above and below the bulk peritectic temperature, respectively. The computed values of λ_L and λ are fairly close, which justifies the adoption of λ_L in this study where an almost analytical approach is available (despite that the using of λ appears to be conceptually more rigorous). For $T > T_{\text{peritectic}}$, both λ_L and λ are divergent as bulk Ni composition approaches the solidus line. For $T < T_{\text{peritectic}}$, λ_L and λ level off at the bulk solvus line (X_{solvus}), above which the bulk chemical potential is a constant (despite any changes in the overall bulk composition in the two-phase region).

Furthermore, lines of constant computed λ_L are plotted in the bulk-phase diagram of the Mo-Ni system (Fig. 5). This is a primitive type of GB diagram where the computed λ_L value represents the thermodynamic tendency for average general Mo GBs to disorder. Note that λ_L (or λ) is not the actual IGF thickness, but it should scale the thickness of the actual IGF. Direct HRTEM measurements[17] showed that the computed λ_L and λ values are good estimations for the average thickness of IGFs at general GBs (see Sec. IIIE and Fig. 11 for a direct comparison).

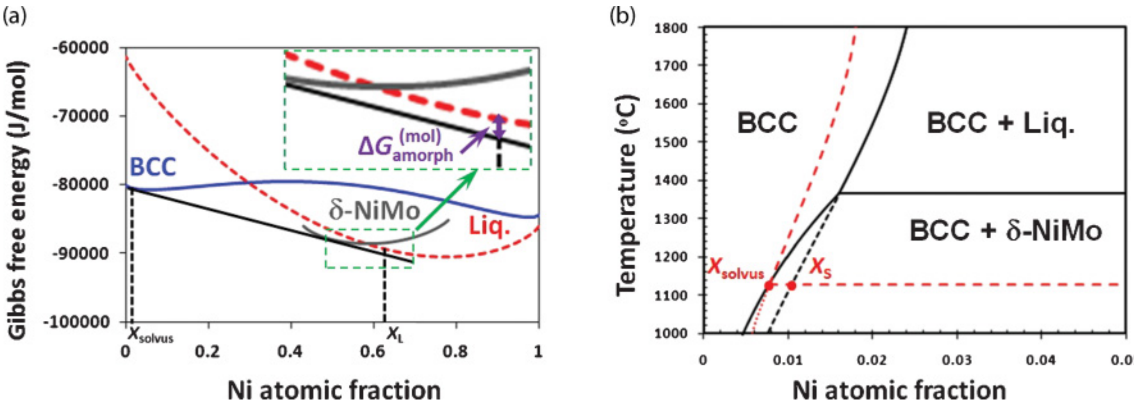

FIG. 3. (Color online) (a) Illustration of $\Delta G_{\text{amorph}}\,(X_L)$ at $T = 1300\,^\circ\text{C}$ in the subperitectic two-phase (BCC + δ) regime. (b) The Mo-rich portion of the corresponding binary bulk-phase diagram. The red dashed line is a line of constant λ_L. In the solid-solid two-phase regime, this line of constant λ_L should be a horizontal line, which can be graphically constructed by finding the intersection of this line of constant λ_L in the single-phase region and the bulk solvus line.

It should be noted that the assumption of $X_{\text{film}} = X_L$ (for computing λ_L) becomes invalid as $X_0 \rightarrow 0$ (for virtually pure Mo).[1,35] However, this is not a major concern for the region of $T \ll T^{\text{Mo}}_{\text{melting}}$ where computed $\lambda_L \ll \xi$ ($\approx$ the atomic size) for nearly pure alloys, indicating that the liquidlike GB structures do not form at all. For pure Mo, λ_L can be estimated as $-\Delta\gamma \cdot [\Delta H^{\text{Mo}}_{\text{fuse}}(T^{\text{Mo}}_{\text{melting}} - T)/T^{\text{Mo}}_{\text{melting}}]$ at temperatures close to the melting point of pure Mo ($T^{\text{Mo}}_{\text{melting}}$) where $\Delta H^{\text{Mo}}_{\text{fuse}}$ is the fusion enthalpy of pure Mo and $\Delta\gamma$ is calculated for pure Mo. Thus, the GB diagram (lines of constant λ_L) can be constructed by interpolation for the region that is close to the melting point of pure Mo, which is illustrated in Fig. 5. This issue does not exist if λ or λ^* [Eq. (10)] is adopted, but λ or λ^* has to be computed numerically.

In summary Figs. 4 and 5 illustrate that the computed λ_L increases with increasing bulk composition in the single-phase region. Above the peritectic temperature the computed λ_L is divergent at the bulk-solidus temperature. Below the peritectic temperature the computed λ_L levels off at the bulk-solvus temperature, and it becomes a constant in the BCC-δ two-phase regime. This computed GB diagram is validated by comparing with a contour map of measured temperature and composition dependent GB diffusivities in Sec. III.

III. EXPERIMENTAL VALIDATION AND DISCUSSION

A. Experimental procedure

In order to validate the computed GB diagram, controlled sintering experiments were conducted to estimate the GB diffusivity as a function of temperature and overall composition. High-purity molybdenum (99.999%) with an average particle size of ~20 microns was purchased from Alfa Aesar. To achieve a homogeneous distribution of nickel in molybdenum, nickel chloride ($\text{NiCl}_2 \cdot 6\text{H}_2\text{O}$, Alfa Aesar) was mixed with molybdenum in solutions. Then the slurries were dried in an oven at 90 °C, annealed in a tube furnace at 600 °C for 1 hour under the flowing gas of Ar + 5% H_2 to reduce nickel chloride to nickel, and pressed into pellets. We assembled a special quench furnace, which was unique in that a mechanism of loading and unloading samples was built to allow the specimens to be rapidly inserted into the hot zone or taken out to the cold zone. Thus, the specimens could be heated to a target temperature in a negligibly short time (~2 minutes). Moreover, after conducting isothermal sintering for a desired duration, the specimens could be cooled down quickly (to below 800 °C in ~1 minute). By doing this the effects of heating and cooling ramps on densification were minimized. In all experiments Ar + 5% H_2 gas was flowing through the tube-furnace system to protect specimens from oxidation, and

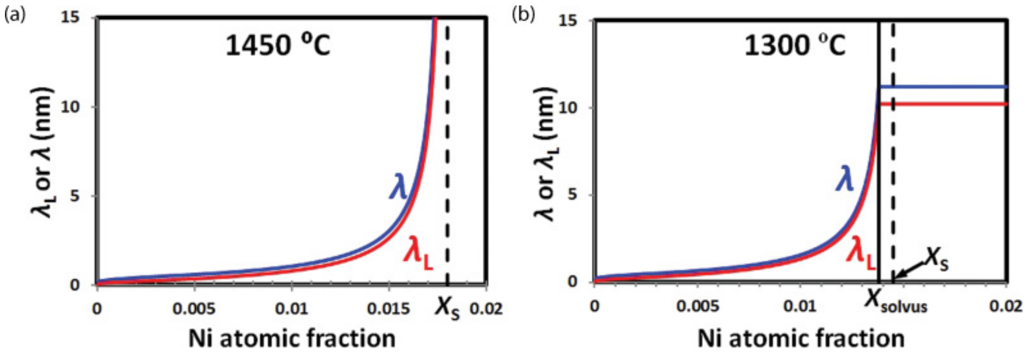

FIG. 4. (Color online) Representative plots of computed λ_L and λ vs Ni-atomic fraction at (a) 1450 °C and (b) 1300 °C, respectively. X_S and X_{solvus} represent bulk solidus and solvus compositions, respectively.

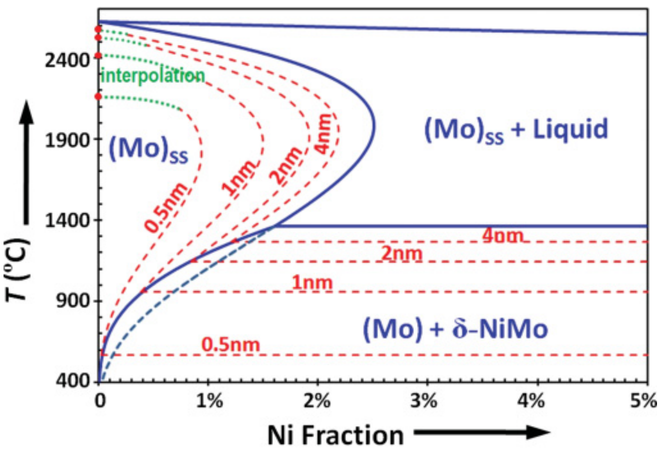

FIG. 5. (Color online) A computed GB diagram (λ diagram) for Ni-doped Mo. The computed lines of constant λ_L are plotted in the Mo-Ni binary bulk-phase diagram to represent the thermodynamic tendency for general Mo GBs to disorder (represented by the red dashed lines; the values of computed λ_L are labeled). The blue dashed line is the metastable extension to the bulk solidus line.

a second thermocouple was placed in the crucible to monitor the actual temperature of the specimens.

We investigated the sintering behaviors in three phase regimes: the solid single-phase regime (BCC), the subperitectic two-phase regime (BCC + a small fraction of the δ phase), and the solid-liquid two-phase regime (BCC + a small fraction of the liquid phase). The relative density vs time curves were measured in isothermal sintering experiments conducted at 50 different conditions (each represented by a specific sintering temperature and an overall Ni content), and these conditions are labeled in the Mo-Ni binary-phase diagram in Fig. 6. Because of a large number of experiments (∼300 experiments conducted at 50 different temperature and composition conditions, multiplied by ∼6 different sintering durations), we could not make and measure multiple specimens for each experiment. Therefore, 3–4 specimens were prepared for a few representative conditions to estimate the typical specimen-to-specimen variations (error bars). The standard deviations were found to be about 0.005 in the relative density or ∼0.0013 in the linear shrinkage ($\Delta L/L_0$). The grain sizes of the samples containing different amount of Ni and sintered at different temperatures were measured by SEM.

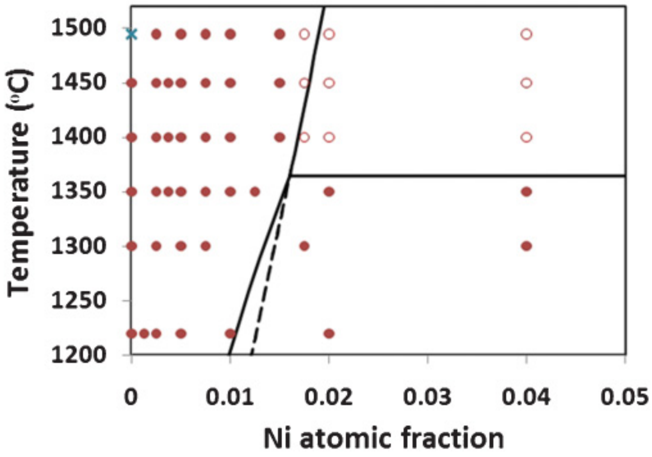

FIG. 6. (Color online) Illustration of the 50 selected experimental conditions in the Mo-Ni phase diagram. The blue cross indicates that the densification is controlled by bulk diffusion, while brown (solid or open) dots indicate that the densification is controlled by GB diffusion. The open dots represent the cases where grain growth cannot be ignored.

B. Densification, grain growth, and sintering mechanism

All plots of relative density vs sintering time curves (raw data) are shown in Fig. 7. These plots show consistent trends: the densification rate generally increases with increasing Ni content or temperature. Then GB diffusivities are estimated by fitting the well-established sintering kinetics models, and the GB diffusivity is determined as a function of temperature and overall composition.

The grain growth is virtually negligible (within the range of experimental errors) for solid-state sintering at moderate doping levels (⩽1.5 at.% Ni) or at low temperatures (⩽1300 °C). The experimental conditions where grain growth is not negligible are indicated by open circles in Fig. 6. Observable grain growth essentially occurs in the region where the formation of a Ni-rich bulk liquid leads to liquid-phase sintering (with a couple of exceptions of solid-state sintering occurring at high temperatures and very close to the solidus line, as shown in Fig. 6). For the regime where the grain growth is not negligible, the effects of grain growth are considered in fitting the sintering models and estimation of errors, which is discussed in the next section.

The GB diffusivity can be estimated from sintering data only if the densification is controlled by GB diffusion. We can determine whether densification is controlled by GB diffusion by obtaining the exponent m for the power law fitting of the initial stage densification kinetics. According to the Johnson model,[45,46] the linear shrinkage in the initial stage follows a power law

$$\frac{\Delta L}{L_0} = \left[K\frac{\gamma_s \Omega D}{kTG^p}\right]^m t^m. \tag{33}$$

If $m = \sim 0.4$–0.5 the densification is controlled by bulk diffusion, and $K = 6$, $p = 3$, and $D = D_{XL}$. If $m = \sim 0.33$ the densification is controlled by GB diffusion, and $K = 12$, $p = 4$, and $D = \delta D_{\mathrm{GB}}$. The exponents ($m$'s) fitted from the raw experimental data shown in Fig. 7 are listed in Table I. This index m is fitted to be 0.44 for pure Mo sintered at 1495 °C; thus, the densification is controlled by bulk diffusion so that GB diffusivity cannot be determined by our experiment (and this particular experimental condition is indicated by the cross in Fig. 6). For all other experimental conditions indicated by the circles in Fig. 6, the indices m are fitted to be 0.2–0.36; thus, the densification is likely be controlled by GB diffusion, for which GB diffusivities can be estimated from the densification vs time curves. This sintering mechanism map obtained in this study (Fig. 6) is consistent with a prior report.[47]

C. Estimation of GB diffusivities

In general the intermediate stage-densification data are the most reliable for estimating the GB diffusivities from fitting

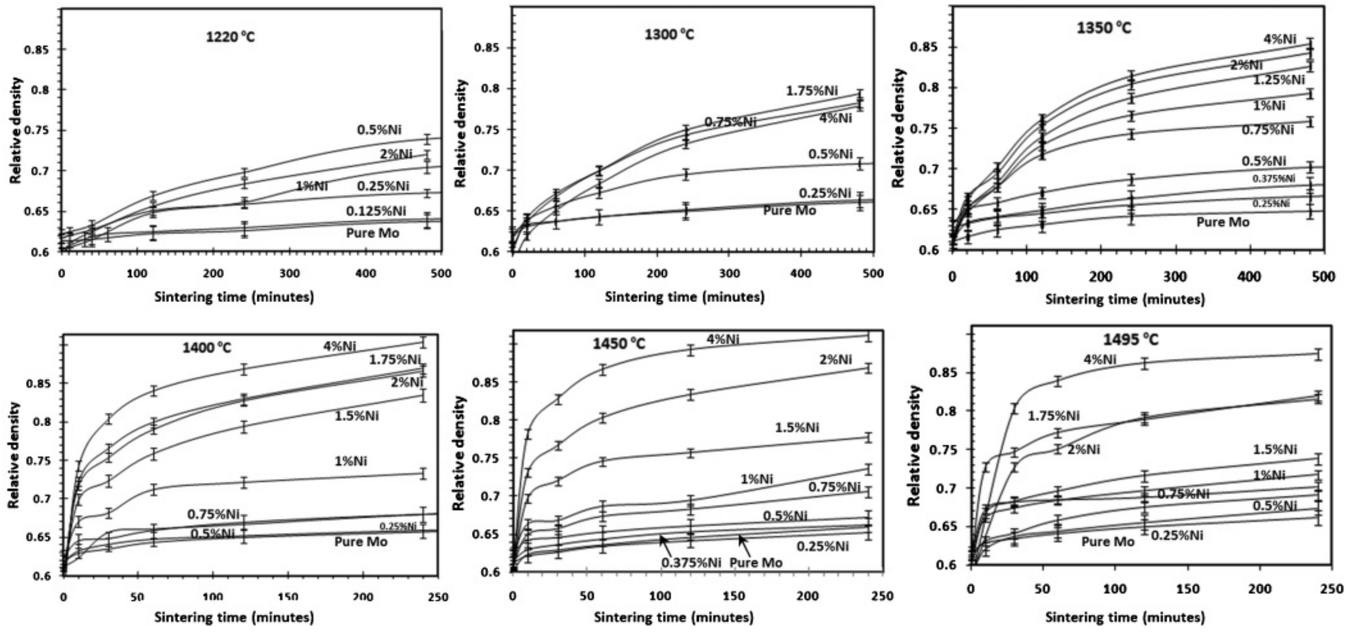

FIG. 7. Plots of relative density vs sintering time at (a) 1220 °C, (b) 1300 °C, (c) 1350 °C, (d) 1400 °C, (e) 1450 °C, and (f) 1495 °C, respectively. The Ni contents are labeled.

densification vs time curves. In the Coble model for the solid-state sintering, the GB-diffusion controlled densification rate in intermediate stage is expressed as[46,48]

$$\frac{d(P^{3/2})}{dt} = -1281\frac{\delta D_{\mathrm{GB}}\gamma_s\Omega}{kTG^4}, \tag{34}$$

where P is the porosity ($P = 1 - \rho_r$; ρ_r is the relative density), D_{GB} is the GB diffusivity, γ_s is the surface energy of Mo (estimated to be ~ 3 J/m^2), Ω is the atomic volume of vacancy (1.56×10^{-29} m^3), k is the Boltzmann constant, and G is the grain size. If the grain size can be assumed to be a constant, integration of Eq. (34) leads to

$$(P)^{3/2} - (P^0)^{3/2} = \left[-1281\frac{\delta D_{\mathrm{GB}}\gamma_s\Omega}{kTG^4}\right]\cdot t. \tag{35}$$

Then the GB diffusivity can be obtained by a linear regression of $P^{3/2}$ vs t.

In some cases where grain growth cannot be neglected, Eq. (34) cannot be integrated directly. The grain-growth kinetics generally obey a power law[49]

$$G^n - G_0^n = A_0 t, \tag{36}$$

where n is usually in the range of 2 to 3 ($n = 2$ in the Turnbull theory).[50] In our sintering experiments of Ni-doped Mo, the measurements show that grain growth obeys the power law of $n \approx 2$, and the previous equation can be rewritten as

$$G^2 = A_0(t + t_0), \tag{37}$$

where $A_0 t_0 = {G_0}^2$. The constants t_0 and A_0 can be obtained by a linear regression. Plugging Eq. (37) into Eq. (34) and integration produce

$$(P)^{3/2} - (P^0)^{3/2} = \frac{1281\delta \cdot D_{\mathrm{GB}}\gamma_s\Omega}{A_0^2 kT}\cdot\left(\frac{1}{t+t_0}\right). \tag{38}$$

Then the GB diffusivity can be obtained by a linear regression of $P^{3/2}$ vs $1/(t + t_0)$.

For pure Mo and a limited number of other cases of low doping-level samples, it is difficult to reach the intermediate stage within a reasonable time. Therefore, we also use the Johnson initial-stage sintering model to estimate the GB diffusivity. For GB diffusion controlled densification, Eq. (33) can be rewritten as

$$\left(\frac{\Delta L}{L_0}\right)^3 = \left(12\frac{\gamma_S\Omega\cdot\delta D_{\mathrm{GB}}}{kTG^4}\right)\cdot t. \tag{39}$$

TABLE I. Exponents (m's) fitted from sintering kinetics.

at.% Ni	0% (pure Mo)	0.25%	0.5%	1.0%	1.5%
1495 °C	0.44 ± 0.06	0.20 ± 0.02	0.23 ± 0.03	0.32 ± 0.02	0.22 ± 0.03
1450 °C	0.31 ± 0.11	0.23 ± 0.03	0.22 ± 0.03	0.29 ± 0.02	0.20 ± 0.03
1400 °C	0.29 ± 0.06	0.24 ± 0.01	0.26 ± 0.02	0.25 ± 0.04	0.23 ± 0.07
1350 °C	0.28 ± 0.03	0.23 ± 0.03	0.31 ± 0.02	0.36 ± 0.03	
1300 °C	0.29 ± 0.06	0.23 ± 0.02	0.28 ± 0.07		
1220 °C	0.29 ± 0.06	0.35 ± 0.03	0.26 ± 0.07	0.33 ± 0.08	

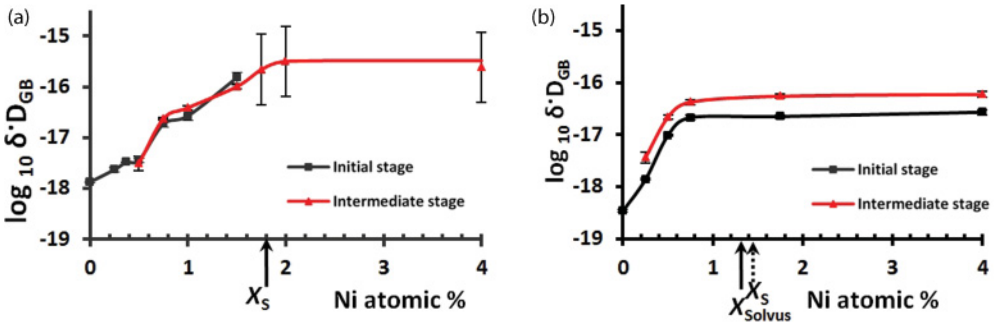

FIG. 8. (Color online) Representative plots of logarithmical GB diffusivity vs Ni-atomic percentage for specimens sintered at (a) 1450 °C and (b) 1300 °C, respectively. The GB diffusivities estimated using initial-stage and intermediate-stage sintering data are shown. The bulk solidus (X_S) and solvus (X_{solvus}) compositions are indicated.

The GB diffusivity can again be obtained by a linear regression. Pre-sintering annealing is applied in our experiments, which resulted in a small shrinkage before isothermal sintering. Although this pre-existing shrinkage is virtually negligible (<1% in all cases), its effect is accounted for by introducing a constant into Eq. (39) for the linear regression (and the validity of this modification is justified by the master sintering curve theory).[51] For a number of conditions we estimated GB diffusivities from both initial-stage (Johnson model) and intermediate-stage (Coble model) densification data, and the obtained results are consistent with each other (see, e.g., Fig. 8).

As shown in Fig. 6 some experiments are conducted in the liquid-phase sintering region. The densification in liquid-phase sintering follows the model that has been developed by Kingery[52] and improved by German.[53] The liquid-phase sintering models are slightly different from the Coble solid-state sintering model[52] attributable to presence of liquid phase and rearrangement process. However, here we apply the Coble solid-state sintering model to fit the liquid-phase sintering data (obtained in experiments where the volume fractions of liquid are small so that the rearrangement is mostly negligible)[52] to estimate nominal GB diffusivities for the sake of fair comparisons.

The random errors in calculating GB diffusivities are generally estimated based on the standard variants of the linear regressions. In cases where grain growth is negligible a systematical error bar is estimated based on the measurement accuracy of grain size, which is labeled in the left-bottom corner in Fig. 9. When grain growth is not negligible, more generous error bars, which are obtained by estimating the upper and lower bounds based on initial and final grain sizes, are given in Figs. 8 and 9.

D. GB diffusivities and model-experiment comparison

In the following section we systematically compare the composition- and temperature-dependent GB diffusivities (estimated from the densification data) with the computed λ values. The computed λ values correlate with GB diffusivities in two ways. First the effective interfacial width (δ or h_{eq}) likely increases with increasing λ. Second an increase in the effective interfacial width will generally result in an increase in the level of structural disorder, which will lead to an increase in D_{GB}. In all cases [Figs. 8, 9, and 10(b)] for this study the estimated values of δD_{GB} are plotted as the effective diffusivities along the GBs. This is the typical way to express GB diffusivities that are related to GB-controlled densification. However, in the context of GB mobility and grain growth, the effective diffusivity perpendicular to this GB is relevant; in such a case the effective interfacial width (δ or h_{eq}) should appear in the denominator.[5,10] Yet, with an increase in λ, we generally expect an increase in the GB mobility because the increase in D_{GB} (in the nominator) should overwhelm the increase in the effective interfacial width (in the denominator).

The effects of the Ni content on GB diffusivities are illustrated by the two representative plots shown in Fig. 8. The GB diffusivity vs Ni-content curve for specimens sintered at 1450 °C [Fig. 8(a)] represents the typical sintering behaviors above the peritectic temperature (1362 °C). Here the estimated

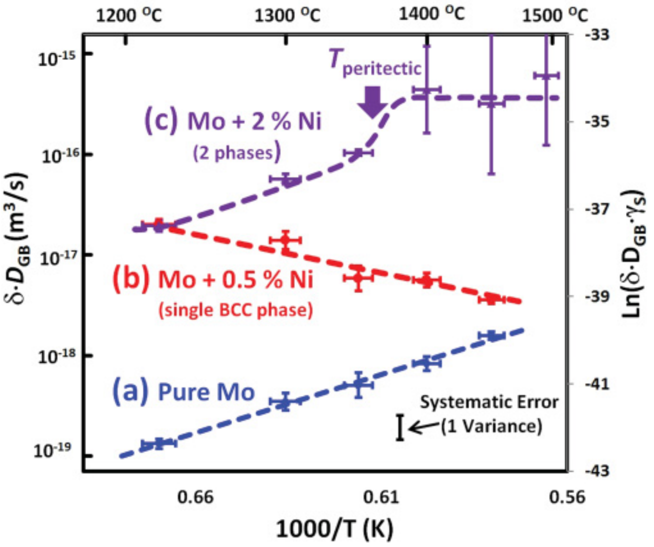

FIG. 9. (Color online) Estimated GB diffusivity ($\delta \cdot D_{\mathrm{GB}}$) vs temperature ($T$) curves for (a) pure Mo, (b) 0.5 at.% Ni-doped Mo (with a single BCC phase), and (c) 2 at.% Ni doped Mo (Ni-saturated Mo). Curves (a) and (b) were published in Ref. 33 and included here for comparison. The diffusivity for the 2 at.% Ni specimen at 1300 °C point is interpolated from the measured diffusivities at the same temperature shown in Fig. 8(b); all other diffusivity data are estimated from the densification vs time curves directly.

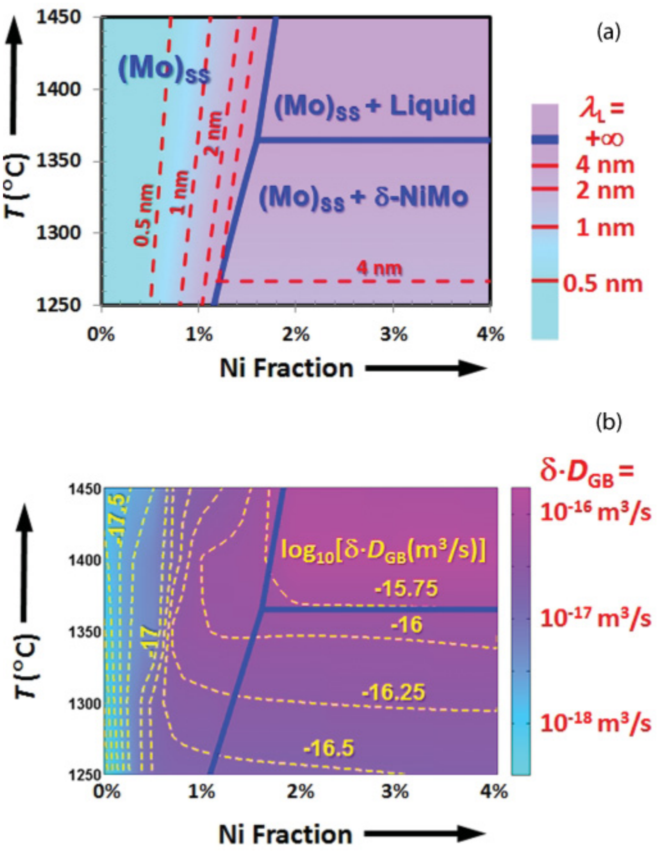

FIG. 10. (Color online) (a) A color version of the GB diagram shown in Fig. 5 that is enlarged to show the area of interest. The diagram is color coded to represent the computed λ_L values, which represent the thermodynamic tendency for general Mo GBs to disorder. (b) A contour map of the experimentally obtained GB diffusivities that are interpolated from the GB diffusivities estimated from sintering experiments.

GB diffusivity increases with increasing Ni content in the single-phase region; above the solidus line ($X_0 > X_S$) the estimated nominal GB diffusivity levels off (noting that in the solid-liquid region, the estimated GB diffusivity is only nominal because the densification no longer follows the solid-state GB-controlled sintering models). This implies that the activated sintering is attributable to the enhanced diffusion in quasiliquid IGFs that are stabilized at GBs below the bulk-solidus line. The formation of premelting-like IGFs in the single-phase region has been directly observed by HRTEM in our prior study.[17] Figure 8(a) also suggests that the formation of a small amount of bulk-liquid phase above the solidus does not significantly improve the densification beyond the solid-state activated sintering rates (that are achieved by diffusion in nanoscale premelting-like IGFs).

When the sintering temperature is below the peritectic temperature, the GB diffusivity increases with increasing Ni content before it levels off. A representative plot obtained from specimens sintered at 1300 °C is shown in Fig. 8(b). In the BCC-δ two-phase region ($X_0 > X_{\text{solvus}}$) the estimated GB diffusivity is virtually a constant (that is independent of the overall composition). This is because the chemical potential is a constant in this region; thus, the equilibrium thickness of the IGFs, which is a function of the chemical potential instead of the overall composition, is a constant in this region. It is interesting to note that the estimated GB-diffusivity levels off below the solvus composition. It is possible that there are some errors in the bulk-solvus compositions obtained from the CalPhaD computation (since this particular bulk-solvus line has not been accurately measured). It is also possible that the presence of some (unknown) interfacial forces restrains the thickening of IGFs below the solvus line.

The three sets of measured GB diffusivity vs temperature curves, which are shown in Fig. 9, provide a further critical validation of the computed GB diagram. First, for pure Mo [Fig. 9(a)], GB diffusivity increases with increasing temperature, which follows a classical thermally activated Arrhenius behavior. Second, as we have reported in a recent letter,[33] the estimated GB diffusivity decreases with increasing temperature [Fig. 9(b)] because of the retrograde solubility of Ni in the Mo-based BCC phase for specimens doped with 0.5 at.% Ni [which exhibit a single BCC $(\text{Mo})_{\text{SS}}$ phase for the temperature range of 1200–1500 °C according to Figs. 5 and 10]. This counterintuitive observation can be well explained by the interplay of the retrograde solubility and GB premelting/prewetting. As shown in Fig. 10(a), the solidus line and its metastable extension exhibit positive slopes in the temperature range of 1200–1500 °C. For a single-phase alloy of a fixed Ni content of 0.5 at.%, this composition moves away from the solidus line with increasing temperature. Consequently the free-energy penalty for forming an undercooled liquid increases, and the general GBs "solidify" with decreasing diffusivity, as being demonstrated in our prior study.[33] Consistently the line of constant λ_L all exhibit positive slopes in Fig. 10(a), i.e., the computed λ_L decreases with increasing temperature for this Mo + 0.5 at.% Ni alloy in this temperature range. Finally, for Mo + 2 at.% Ni specimens (saturated with Ni), where either a solid (δ) or liquid secondary phase is present (see Fig. 10), the estimated GB diffusivity increases with increasing temperature until it levels off at and above the peritectic temperature [Fig. 9(c)]. Again these experimental observations are consistent with the computed GB diagram and λ_L values.

To systematically validate the computed GB diagram and the underlying interfacial thermodynamic models, the computed GB diagram shown in Fig. 5 is enlarged to zoom in the temperature and composition area where experiments were conducted. This enlarged diagram is shown in Fig. 10(a) and color coded to represent the computed λ_L values or thermodynamic tendency for general Mo GBs to disorder. On the other hand we construct a contour map of experimentally estimated GB diffusivities, which is interpolated from the GB diffusivities extracted from intermediate-stage sintering data (except for the GB diffusivities for pure Mo, which are estimated from initial-stage sintering data). This diagram is shown in Fig. 10(b), which is color coded to represent the values of the estimated GB diffusivities. The trends of the measured GB diffusivity as a function of temperature and the overall Ni content [as shown in Fig. 10(a)] correlate well with the computed GB diagram shown in Fig. 10(a). This represents the most systematical validation of a computed GB diagram (λ diagram), and it demonstrates the validity and predictability of the proposed interfacial thermodynamic models, as well as

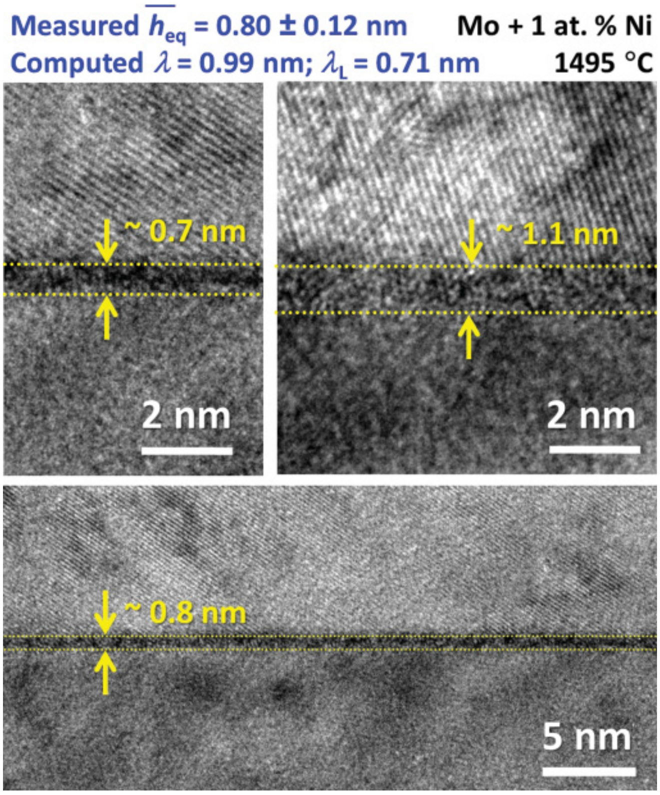

FIG. 11. (Color online) Comparison of the average measured thickness vs computed λ values for a Ni + 1 at.% Ni specimen quenched from 1495 °C. The measured thicknesses exhibit a boundary-to-boundary variation, and computed λ values represent rough estimations of the interfacial widths for the average general GBs (without considering the interfacial interactions). The experimental procedure was reported in Ref. 17, but these HRTEM images shown here were not reported in the prior letter.

usefulness of such a computed λ diagram in forecasting the trends of sintering (and presumably other relevant fabrication processing and materials properties).

E. Rigorous GB "phase" diagrams and Dillon-Harmer complexions

We should emphasize that the computed values of λ_L and λ are rough estimations of the effective interfacial widths considering neither the details of interfacial interactions nor the boundary-to-boundary variation. Nonetheless Fig. 11 shows that computed values of λ_L and λ are rather good estimations of the effective interfacial width of general GBs. In this case, the measured average IGF thickness is 0.80 nm (with a standard deviation of 0.12 nm) for a 1 at.% Ni-doped Mo specimen that was equilibrated and quenched from 1495 °C (Fig. 11).[17] This is consistent with the model predictions where the λ_L and λ are computed to be 0.71 nm and 0.99 nm, respectively. Moreover, Fig. 11 also shows the boundary-to-boundary variation of the measured IGF thicknesses, which is presumably related to the different crystallography (misorientation and inclinations) of different general GBs in a polycrystalline specimen.

We should further point out that the computed λ diagrams [such as that shown in Figs. 5 and 10(a)] are not rigorous GB "phase" diagrams with well-defined GB-transition lines. Diffuse-interface models have demonstrated the existence of abrupt (first-order) interfacial "phase" transitions at GBs.[7,34,54] Furthermore, phenomenological models[12,28,32,55] showed that an atomic-size effect can produce a series of discrete GB phases (which are called Dillon-Harmer complexions)[5,10,11,55–57]: namely, intrinsic/clean GBs, monolayers, bilayers, trilayers, nanoscale IGFs (with a continuous equilibrium thickness on the order of 1 nm), and complete wetting films (with an arbitrary thickness). The origin of this series of discrete GB "phases" can be well understood via an analogy to layering transitions in a case of multilayer surface adsorption on attractive/inert substrates.[3]

The current model cannot directly predict the formation of these discrete GB phases (Dillon-Harmer complexions), which are dictated by the detailed interfacial interactions that are not represented in the current model. In many cases it is reasonable to expect the formation of discrete monolayers, bilayers, or trilayers when the estimated interfacial width is on the order of 1–3 monolayers. However, like a case of multilayer gas adsorption on inert surfaces,[3] discrete GB phases may form only before the roughening transitions take place; this has been demonstrated for GBs via a thermodynamic model.[28] Moreover, the computed λ value is only a rough estimation of interfacial width (without considering interfacial interactions). Finally the computed λ value represents the thermodynamic tendency for an average general GB to disorder; in a real polycrystal first-order GB transitions are expected to occur at different temperatures (or compositions) at GBs of different crystallography.[12]

In summary the current model and computed λ diagrams cannot predict the exact conditions for formation of each of the discrete GB phases (Dillon-Harmer complexions). In principle if the exact form of interfacial coefficient defined in Eq. (4) is known, the GB-transition lines can be predicted and the rigorous GB "phase" (complexion) diagrams can be constructed. Future studies are needed to quantify the interfacial interactions, which will require the development of more sophisticated and realistic statistical and atomistic models.

IV. CONCLUDING REMARKS

Quantitative interfacial thermodynamic models for binary alloys have been established and applied to the Mo-Ni system. A primitive type of GB diagram (called λ diagram) was constructed for the Ni-doped Mo, where lines of constant λ_L were plotted in the bulk Mo-Ni diagram to represent the thermodynamic tendency for average general GBs to disorder. To systematically validate this computed λ diagram, temperature- and composition-dependent GB diffusivities were estimated from densification vs time curves in a set of controlled sintering experiments. The results were consistent with model predictions, showing the predictability and usefulness of the computed λ diagram.

The model-experimental agreement also critically supports the existence and importance of the coupled GB premelting and prewetting phenomena in binary alloys. The systematical correlation between the temperature- and composition-dependent GB diffusivities and the computed λ diagram reconfirms the previously proposed mechanism of subsolidus (solid-state) activated sintering,[13,16,29] i.e., the enhanced densification could be attributed to the boosted GB diffusion in the premelting-like quasiliquid IGFs that are stabilized below the bulk solidus line where the bulk liquid phase is not yet stable.

This study also demonstrates that the bulk-phase diagrams are not adequate for predicting sintering behaviors, and (presumably) other GB-controlled fabrication processing and materials properties. Thus, it is necessary to develop GB (phase) diagram as a general materials science tool. Although they are not yet rigorous GB "phase" diagrams with well-defined transition lines, the λ diagrams developed in this study can be robustly useful to predict the trends of temperature and composition dependent GB structural disordering. Such information is useful in understanding and controlling sintering; grain growth; GB embrittlement; and GB-controlled creep, corrosion, and oxidation resistance.

Several future studies should be conducted to further extend and validate the models and methods to construct such λ diagrams as well as more sophisticated and rigorous GB "phase" diagrams. Specifically we should extend the models to multicomponent alloys where interactions of multiple dopants may result in more complex interfacial phenomena, as well as ceramic materials where the presence of significant van der Waals London dispersion forces and electrostatic interactions (space charges) will add further complexity. More realistic models and experimental methods to quantify relevant interfacial energies and bulk thermodynamic parameters are also essential for making the computed GB diagrams more accurate and practically useful. Completing these challenging tasks can help to develop realistic GB (phase) diagrams, which can be used as a general materials science tool for mechanism-informed materials design.

ACKNOWLEDGMENTS

This study is primarily supported by AFOSR Grant Nos. FA9550-10-1-0185 and FA9550-07-1-0125 in the High Temperature Aerospace Materials program (monitored by Joan Fuller and Ali Sayir).

---

[*] Currently with TDK Headway Technologies, 682 S. Hillview Drive, Milpitas, CA 96035.

[†] Corresponding author. jluo@alum.mit.edu

[1] J. G. Dash, A. M. Rempel, and J. S. Wettlaufer, Rev. Mod. Phys. **78**, 695 (2006).

[2] J. W. Cahn, J. Chem. Phys. **66**, 3667 (1977).

[3] R. Pandit, M. Schick, and M. Wortis, Phys. Rev. B **26**, 5112 (1982).

[4] A. M. Alsayed, M. F. Islam, J. Zhang, P. J. Collings, and A. G. Yodh, Science **309**, 1207 (2005).

[5] S. J. Dillon, M. Tang, W. C. Carter, and M. P. Harmer, Acta Mater. **55**, 6208 (2007).

[6] B. B. Straumal and B. Baretzky, Interface Sci. **12**, 147 (2004).

[7] M. Tang, W. C. Carter, and R. M. Cannon, Phys. Rev. Lett. **97**, 075502 (2006).

[8] J. Luo, Crit. Rev. Solid State Mater. Sci. **32**, 67 (2007).

[9] J. Creuze, F. Berthier, R. Tetot, and B. Legrand, Phys. Rev. Lett. **86**, 5735 (2001).

[10] M. P. Harmer, J. Am. Ceram. Soc. **93**, 301 (2010).

[11] M. P. Harmer, Science **332**, 182 (2011).

[12] J. Luo, Curr. Opin. Solid State Mater. Sci. **12**, 81 (2008).

[13] V. K. Gupta, D. H. Yoon, H. M. Meyer III, and J. Luo, Acta Mater. **55**, 3131 (2007).

[14] J. Luo, H. Cheng, K. Meshinchi Asl, C. J. Kiely, and M. P. Harmer.

[15] V. Jayaram and R. Sinclair, J. Am. Ceram. Soc. **66**, C137 (1983).

[16] J. Luo, V. K. Gupta, D. H. Yoon, and H. M. Meyer, Appl. Phys. Lett. **87**, 231902 (2005).

[17] X. Shi and J. Luo, Appl. Phys. Lett. **94**, 251908 (2009).

[18] O. Gutfleisch, M. A. Willard, E. Brück, C. H. Chen, S. G. Sankar, and J. P. Liu, Adv. Mater. **23**, 821 (2011).

[19] S. Divinski, M. Lohmann, C. Herzig, B. Straumal, B. Baretzky, and W. Gust, Phys. Rev. B **71**, 104104 (2005).

[20] E. I. Rabkin, V. N. Semenov, L. S. Shvindlerman, and B. B. Straumal, Acta Metall. Mater. **39**, 627 (1991).

[21] O. I. Noskovich, E. I. Rabkin, V. N. Semenov, B. B. Straumal, and L. S. Shvindlerman, Acta Metall. Mater. **39**, 3091 (1991).

[22] J. Luo and Y.-M. Chiang, Annu. Rev. Mater. Res. **38**, 227 (2008).

[23] A. Avishai, C. Scheu, and W. D. Kaplan, Acta Mater. **53**, 1559 (2005).

[24] C. Scheu, G. Dehm, and W. D. Kaplan, J. Am. Ceram. Soc. **84**, 623 (2000).

[25] M. Baram and W. D. Kaplan, J. Mater. Sci. **41**, 7775 (2006).

[26] A. Avishai and W. D. Kaplan, Acta Mater. **53**, 1571 (2005).

[27] M. Baram, D. Chatain, and W. D. Kaplan, Science **322**, 206 (2011).

[28] J. Luo, Appl. Phys. Lett. **95**, 071911 (2009).

[29] J. Luo, H. Wang, and Y.-M. Chiang, J. Am. Ceram. Soc. **82**, 916 (1999).

[30] H. Wang and Y.-M. Chiang, J. Am. Ceram. Soc. **81**, 89 (1998).

[31] H. D. Ackler and Y.-M. Chiang, J. Am. Ceram. Soc. **80**, 1893 (1997).

[32] J. Luo and X. M. Shi, Appl. Phys. Lett. **92**, 101901 (2008).

[33] X. Shi and J. Luo, Phys. Rev. Lett. **105**, 236102 (2010).

[34] Y. Mishin, W. J. Boettinger, J. A. Warren, and G. B. McFadden, Acta Mater. **57**, 3771 (2009).

[35] J. Mellenthin, A. Karma, and M. Plapp, Phys. Rev. B **78**, 184110 (2008).

[36] N. Eustathopoulos, M. Nicholas, and B. Drevet, *Wettabilty at High Temperatures* (Pergamon, Amsterdam, 1999), p. 184.

[37] R. Benedictus, A. Böttger, and E. J. Mittemeijer, Phys. Rev. B **54**, 9109 (1996).

[38] L. P. H. Jeurgens, Z. M. Wang, and E. J. Mittemeijer, Int. J. Mater. Res. **100**, 1281 (2009).

[39] I. Shimizu and Y. Takei, Physica B-Condensed Matter **362**, 169 (2005).

[40] I. Shimizu and Y. Takei, Acta Mater. **53**, 811 (2005).

[41] P. Wynblatt and D. Chatain, Metall. Mater. Trans. A **38A**, 438 (2007).

[42] C. Antion and D. Chatain, Surf. Sci. **601**, 2232 (2007).

[43] K. Frisk, CALPHAD—Computer Coupling of Phase Diagrams and Thermochemistry **14**, 311 (1990).

[44] S. H. Zhou, Y. Wang, C. Jiang, J. Z. Zhu, L. Q. Chen, and Z. K. Liu, Mater. Sci. Eng. A **397**, 288 (2005).
[45] D. L. Johnson, J. Appl. Phys. **40**, 192 (1969).
[46] S. Kang, *Sintering: Desification, Grain Growth & Microstructure* (Elsevier Butterworth-Heinemann, Burlington, Massachusetts, 2004), pp. 37–68.
[47] J. T. Smith, J. Appl. Phys. **36**, 595 (1965).
[48] R. L. Coble, J. Appl. Phys. **32**, 787 (1961).
[49] W. R. Rao, A. D. Jatkar, and G. S. Tendolka, Int. J. Powder Metall. **6**, 65 (1970).
[50] D. Turnbull, Trans. AIME **191**, 661 (1951).
[51] S. J. Park, S. H. Chung, J. M. Martin, J. L. Johnson, and R. M. German, Metall. Mater. Trans. **39A**, 2941 (2008).
[52] W. D. Kingery, J. Appl. Phys. **30**, 301 (1959).
[53] R. M. German, *Liquid Phase Sintering* (Plenum Press, New York, 1985), pp. 65–90.
[54] M. Tang, W. C. Carter, and R. M. Cannon, Phys. Rev. B **73**, 024102 (2006).
[55] S. J. Dillon, M. P. Harmer, and J. Luo, JOM **61**, 38 (2009).
[56] S. J. Dillon and M. P. Harmer, Acta Mater. **55**, 5247 (2007).
[57] S. J. Dillon and M. P. Harmer, J. European Ceram. Soc. **28**, 1485 (2008).